Counter-helical magnetic flux ropes from magnetic reconnections in space plasmas

Ying-Dong Jia[1], Yi Qi[2], Xueyi Wang[3], Nathan Miles [1,4], C. T. Russell[1], Hanying Wei[1]

1 Department of Earth, Planetary, and Space Sciences, University of California, Los Angeles, CA, USA

2 Laboratory for Atmospheric and Space Physics, University of Colorado Boulder, Boulder, CO, USA

3 Physics Department, Auburn University, Auburn, AL, USA

4 Cooperative Institute for Research in Environmental Sciences, Boulder, CO

Abstract

Magnetic flux ropes are ubiquitous in various space environments, including the solar corona, interplanetary solar wind, and planetary magnetospheres. When these flux ropes intertwine, magnetic reconnection may occur at the interface, forming disentangled new ropes. Some of these newly formed ropes contain reversed helicity along their axes, diverging from the traditional flux rope model. We introduce new observations and interpretations of these newly formed flux ropes from existing Hall Magnetohydrodynamics model results. We first examine the time-varying local magnetic field direction at the impact interface to assess the likelihood of reconnection. Then we investigate the electric current system to describe the evolution of these structures, which potentially accelerate particles and heat the plasma. This study offers novel insights into the dynamics of space plasmas and suggests a potential solar wind heating source, calling for further synthetic observations.

Plain language summary

This research examines a special type of systematically twisted magnetic fields, known as flux ropes, in the sun's atmosphere, the solar wind, and near planets. This examination brings new understanding of how these special flux ropes emerge from collisions between flux ropes are built on earlier model results. These results use a commonly used simulation tool for large-scale plasmas to study the new ropes formed after two flux ropes are pushed toward each other long enough. In some cases, each of the new ropes may have opposite twists between their two ends. We then examine how the magnetic field changes across the interface during the evolution.

Changes in electric currents found in these situations further explain the formation and evolution of the new rope pairs. This examination helps to better understand the behavior of space plasma's heating of the solar wind and its control of space weather.

Key points:

- We examine the interaction of magnetic flux ropes that consist of opposite helicity along their axis using numerical simulations.
- We present the evolution of their current system, from which we anticipate a significant amount of energy release.
- These structures could be present on the solar surface, in solar wind, and magnetospheres.

1. Introduction

Magnetic flux ropes (MFRs), certain "flux tubes" characterized by systematically twisted magnetic fields, are pervasive in space plasmas across macroscale and mesoscales (e.g., Hu et al., 2018). Their presence extends beyond coronal mass ejections (CMEs) in the corona (Gopalswamy, 2004), to interplanetary CMEs (ICMEs) in the inner heliosphere (Howard et al., 2009) and flux transfer events (FTEs) in planetary magnetospheres (e.g. Jia et al., 2010; Lai et al., 2012; Belenkaya et al., 2013). Despite their wide range of plasma and field parameter values in various environments, many MFRs are thought to originate from magnetic reconnections (e.g., Russell & Elphic, 1979a; Moore and Labonte, 1980). Once formed, MFRs are stable and typically display a systematic rotation in their magnetic field vectors, a characteristic readily identifiable in in-situ magnetic field data (Burlaga et al., 1981).

Magnetic helicity, a measurement of such rotation signatures, quantifies the relationship between the axial and azimuthal fields in MFRs. In space plasmas, helicity is considered as a conserved quantity, even amidst dissipation processes like magnetic reconnection. For instance, the helicity dissipation time in a typical coronal loop exceeds 10^5 years (Berger and Field, 1984). Such a conservation principle has encouraged decades of efforts to compare ICME properties with their associated solar surface regions (Bothmer and Rust, 1997, Ulrich et al., 2018, Pal, 2022). In addition, the generation (Forbes and Priest, 1995; Qiu et al., 2007), distribution (see De Keyser et al., 2005, Chapter 8.6), and transport (Berger and Field, 1984; Manchester et al., 2017) of helicity in (I)CMEs have been extensively investigated. When ICMEs pass by Earth, they are

believed to significantly affect magnetospheric activities, with such impacts largely dependent on their helicity (e.g., McAllister 2001).

In Earth's magnetosheath, the disentanglement process of colliding MFRs has been observed in Magnetospheric Multiscale (MMS) data (e.g. Qi et al., 2020), resolving a long-standing issue concerning the evolution of interlaced MFRs (e.g. Hesse et al., 1990). Back to the interplanetary space, similar processes are then hypothesized to explain Magnetic Increases with Central Current Sheets (MICCSs) by Fargette et al., (2021). Subsequently, numerical models have been developed to simulate MFR collisions, successfully replicating these disentanglement processes in both the magnetosphere and interplanetary solar wind (Jia et al., 2021; 2023). In some of these model results, we noticed the formation of a new type of MFRs containing the helicity of opposite signs along a single rope, namely counter-helical MFRs (CHFRs). This phenomenon is determined by the initial chirality of these colliding MFR pairs and the local plasma conditions at the interface.

On the solar surface, the existence of CHFRs can be found in some numerical simulation results but not thoroughly examined (Linton et al., 2001; Torok et al., 2011). They are also proposed for some erupting CMEs, as inferred from spacecraft imagery (Thompson, 2013). Nonetheless, due to their unstable nature and scarcity of concurrent observations to date, extensive studies of MFRs with differing helicities in the solar wind and magnetospheres have been limited, except for erosion studies (e.g. Pal et al., 2021), prompting a synthetic investigation.

In section 2, we reexamine prior numerical models and their outcomes to introduce a particular type of formation of CHFR mechanisms. We detail the magnetic field configurations during their formation process to evaluate the conditions necessary for their production during such processes. In section 3, we analyze the evolution of the associated current system and estimate the energy release of CHFRs. By analyzing various interaction scenarios, our comprehensive study substantiates the formation and evolution of CHFRs. We also highlight their significance and advocate for further observational research in the solar wind and magnetospheres.

2. Model and results

A pair of interlaced flux ropes (IFRs) within the context of a typical 1 AU solar wind is adopted as the initial condition in our time-dependent interaction model. The solar wind

parameters are listed in Table 1. Each MFR is formulated by the force-free cylindrical model (Lundquist, 1950):

$$B_{r'}=0,\ B_{\varphi'} = HB_0J_1(\alpha r'/R_0),\ B_{z'}= B_0J_0(\alpha r'/R_0) \text{ when } r' \le R_0$$
$$B = 0 \text{ when } r' > R_0 \quad (1)$$

Here, r', φ', and z' represent local poloidal coordinates centered at the MFR. Functions J_0 and J_1 are the 0th and 1st-order Bessel functions, respectively. Constant R_0 = 130Mm is the radius of the MFR, and the constant $\alpha = 2.405$ is the first 0 point of J_0, dropping the axial field to zero at the MFR surface. These components are then transferred into B_x, B_y, and B_z in the Cartesian coordinate of the simulation domain, as shown in Figure 1. The rope axis z' is set parallel to the z-axis for the left MFR (initial displacement x_{L0} = 160Mm) and to the y-axis for the right MFR (x_{R0} = −160Mm), causing an impact angle of 90°. Comparable to the background interplanetary magnetic field (IMF), we set the axial field B_0 = 13nT. The parameter H=±1 denotes the chirality of the helical magnetic vectors of each MFR: When H = 1, the MFR is right-handed.

During the evolution, it is anticipated that the plasma flow will drive the two MFRs to collide, creating an interface at the origin, as depicted in Figure 4 by Jia et al. (2021). For the two MFRs to successfully disentangle, magnetic reconnection must occur rapidly at this interface. When variations in other factors are negligible, the rate between the guide field and the reconnecting field has been found to govern the efficiency of magnetic reconnections using models and lab experiments (Pritchett & Coroniti, 2004; Lu et al., 2011; Tharp et al., 2012). We note that the difficulty of verifying this trend with space measurements is reviewed by Genestreti et al. (2018).

To assess the guide field and thereby the likelihood of MFR reconnection, we examine the magnetic field across the interface before presenting the self-consistent simulation results. In our conceptualization, we assume that the two MFRs move with the driving plasma flow and interpenetrate, without experiencing deceleration or deformation. As they overlap, different parts of the MFRs reach the interface at various stages: The side with the smallest x-coordinate of the MFR on the left will arrive early, while the part with the largest x-coordinate in this MFR will arrive later (red arrows in Figure 1). Under this assumption, we use the local field within the MFRs to depict the field arrows across the interface. Both the early (before reconnection) and late (after reconnection) stages of this hypothetical interpenetration are sketched in the same 3-D projection in Figure 1.

At the early stage of the hypothetical collision, the magnetic fields in the L-R case (Figure 1a) exhibit a large shear angle, promoting reconnection. In contrast, the magnetic field vectors in the L-L case (Figure 1b) are nearly parallel, leading to a strong guide field that hinders reconnection. Conversely, in the later stages of these IFRs, both cases exhibit a significant angle between field vectors, potentially facilitating reconnection.

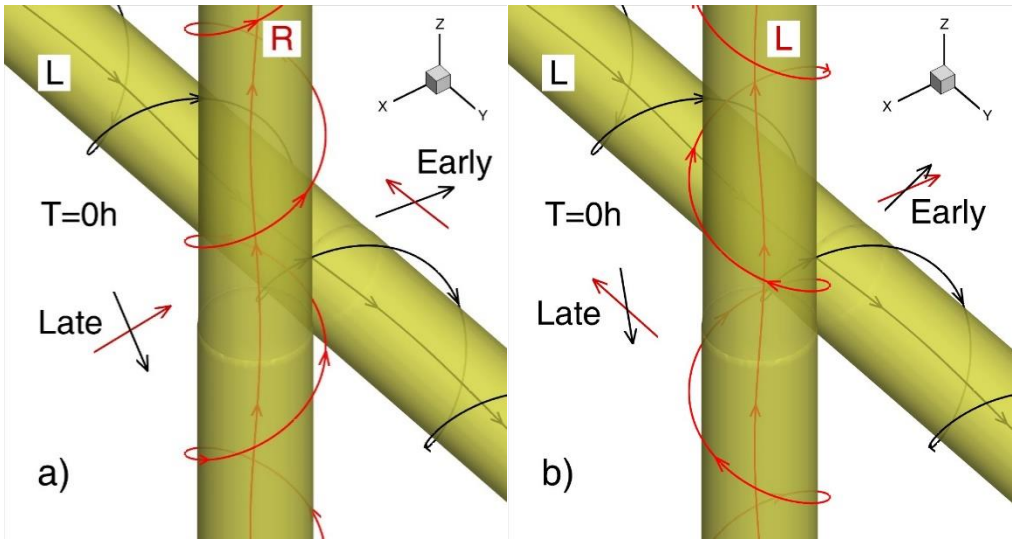

Figure 1. Three-dimensional view of the initial conditions (T=0h) of two distinct simulation cases. The black and red curves represent magnetic field lines, spiraling around the yellow cylinders representing the MFRs. Chirality in the MFRs (L-R, L-L) is indicated by the letters labeled. After this T=0 stage, field arrows are sketched during a hypothetical interpenetration. Black arrows represent B vectors from the left MFR side (x<0 initially), while red arrows are from the right MFR (x>0 at T=0).

Two plasma flows, each with a speed of $u = u_x = \pm 13$ km/s, are driven against each other, maintained by boundary conditions, as shown by the color contours in Figure 2. A 3-D Hall MHD version (Toth et al., 2008) of the BATS-R-US code (Toth et al., 2012) is used to simulate this process. Additional details regarding the L-R case, employing the same solar wind condition, are provided in a recently submitted paper focusing on enhancements in the interplanetary magnetic field (Jia et al., 2023).

Table 1. Selection of parameters in models for two distinct space plasma regimes.

	Solar wind	Magnetosheath
n (/cc)	5	10
T (K)	5e5	2e7
B_0 (nT)	12	29
Domain size X_{max} (Mm)	2000	160
Grid size Dx (Mm)	16	0.3
MFR radius R0 (Mm)	130	2.5
Time For L-R case to disentangle	17h	40 min

The solar wind IFR model results with the L-R and L-L configurations are illustrated in Fig. 2. Panels a and b show the evolution of the L-R case. At T=10h, a pair of new MFRs is forming when left-handed MFRs are connecting to right-handed MFRs. At T=17 hours shown in Fig. 2b, the pair of new MFRs are liberated, each having opposite helicity on their two ends, to form a pair of CHFRs as sketched in panel c.

In contrast, the L-L case shown in panel d remains entangled at 17h, due to the strong guide field at its early stage. Additional simulations were conducted with varying plasma temperatures between 5e5 and 1e7 K for this L-L case, but disentanglement did not occur in any of these scenarios. The outcome of both cases is consistent with our earlier field vector analysis of the early stage shown in Figure 1.

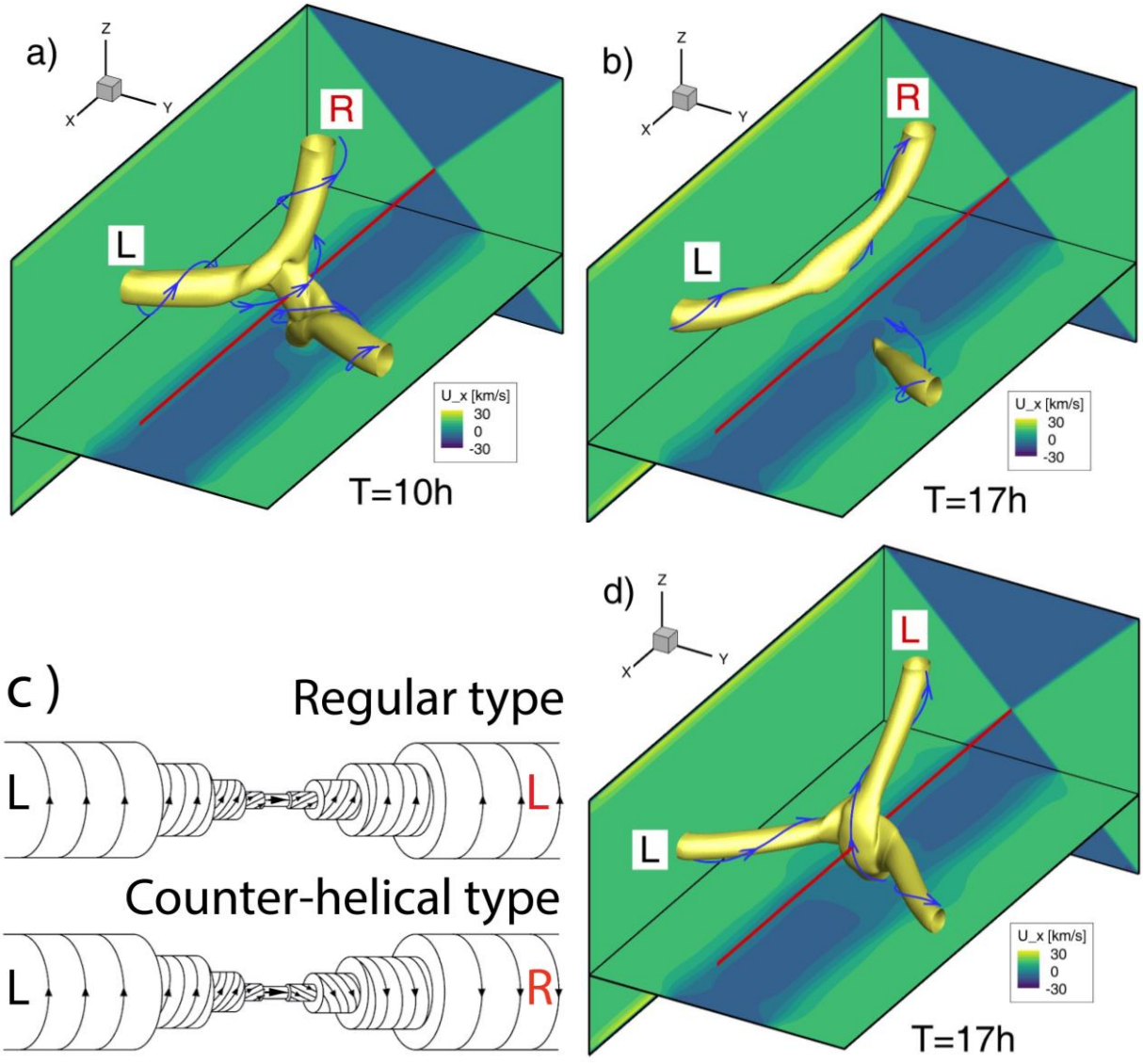

Figure 2. Three-dimensional plots comparing the simulation results of L-R (panels a, b) and L-L (panel d) cases. Panels a and b show the same model result plotted in their Figure 4 by Jia et al. (2023). The blue curves depict field lines winding around the yellow cylinders that represent the MFRs. Color contours illustrate the ion speed component u_x are located at planes defined by x= –2000, y= –1000, and z= –360 Mm, respectively. The red line in the center denotes the x-axis. Panel c sketches a counter-helical MFR and compares it with a regular MFR reproduced from Fig.3 by Russell and Elphic (1979b).

Utilizing the same code, Jia et al. (2021) simulated a comparable process in the Earth's magnetosheath, with the corresponding parameters also detailed in Table 1. Disentanglement

occurred in both the L-R and L-L cases. However, the disentanglement process took over 100 minutes for the L-L case, whereas it only required 40 minutes for the L-R case, also consistent with our vector analysis. To explore kinetic effects during this process, we subsequently replicated the L-R case in the magnetosheath using a hybrid code (Wang et al., 2009), yielding consistent results (not shown here). We advocate for additional simulations employing these computationally intensive kinetic codes to improve the accuracy of our magnetic reconnection modeling.

3. Discussion and conclusions

Along the axis of an MFR, the axial field's polarity remains constant due to the solenoidal nature of the magnetic field vector **B**. In our IFR scenario, this principle dictates the linkage in the new pair of MFRs: A disconnected half of the original MFR must pair with the MFR half that contains the same axial field. For a L-R case, the –y half must connect to the +z half, instead of the –z half. Consequently, the segments of opposite helicity are connected. Helicity is also an indicator of another solenoidal vector: The electric current density vector **j** (Russell and Elphic, 1979b). For this L-R case, we are thus faced with an apparent dilemma: How do these pairs of half MFRs carrying opposite **j** connect, without violating the divergence-free requirement of **j** under MHD assumptions? To resolve this, we examine these current systems.

The left panel of Figure 3 shows the initial current system of MFRs in the L-R case, calculated from the analytical force-free solution (equation 1). The y-component of current is plotted in color contours on the two plane slices, with the black curves marking $j_y = 0$. At $x<0$ as an example, the radius of the outer black curve is R_0, which coincides with the MFR radius. The radius of the inner circle is $r_1 = 1.841R_0/\alpha$, corresponding to the first peak of the Bessel function $J_1(r')$. As shown on both planes, $j_y > 0$ when $r_1 < r' < R_0$ in a surface region, and $j_y > 0$ when $0 < r' < r_1$ in the core region, indicating the reversal of the axial component of the current in this MFR.

We further illustrate this current system in 3-D with color-coded streamlines. This current reversal is further illustrated by the two colors assigned to the streamlines of **j**, differentiating the surface current from the core current. In the case of the right-handed MFR at $x>0$, the core current has the same sign as the poloidal field B_y (white lines), while the surface **j** has the opposite sign (cyan line). This r'-sign relationship inverts when $H = -1$, in the left-handed MFR at $x>0$. On the other hand, we note that although the surface current is clustered in a thin layer to

compensate for all the core current, their directions still satisfy the **j** = c**B** nature of a force-free field: **j**(R0) = $\mathbf{j}_\varphi$ (not shown), where c is a scalar.

Such a surface-core current system occurs because the total current flux in a force-free MFR equals zero (Solov'ev & Kirichek, 2021), a characteristic also derivable from our Eq. 1. Consequently, when a counter-helical flux rope (CHFR) forms, these currents can close at any cross-section by connecting the two oppositely flowing currents to conserve the total current flux. This is illustrated by the two self-winding curves in the right panel of Figure 3, which shows the later stage of the disentanglement process. In the left-handed segment, the surface current (white) flows in the axial B direction and then connects to the core current that flows backward (cyan). In summary, this $\nabla\cdot\mathbf{j}$=0 dilemma is resolved by the self-closure of surface and core currents in such originally force-free structures.

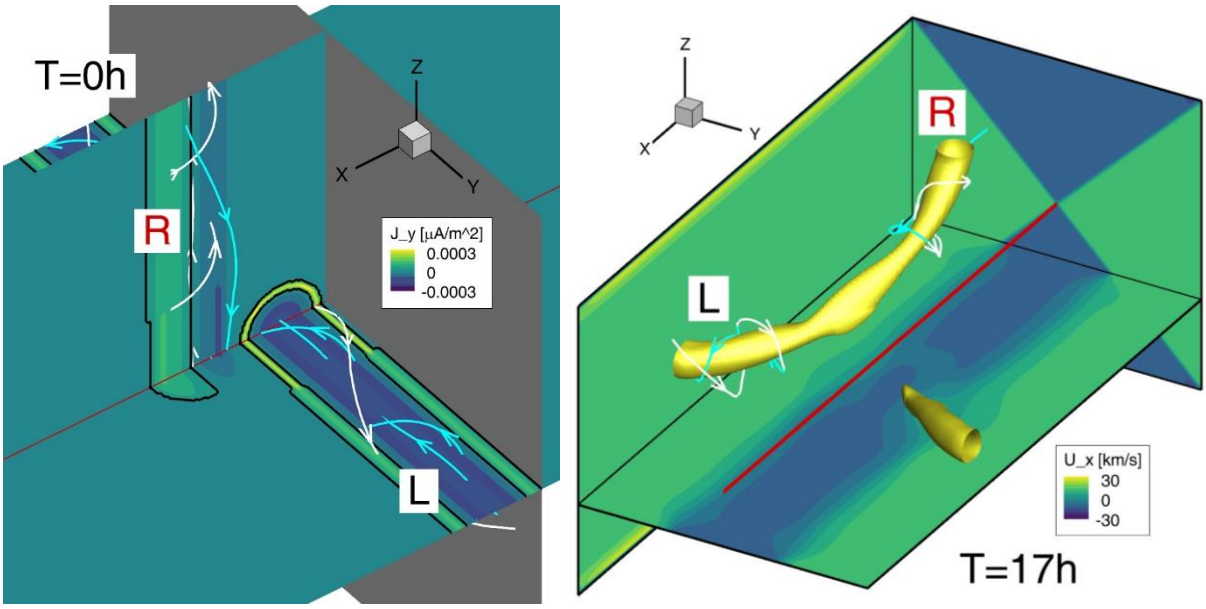

Figure 3. Three-dimensional plots of the L-R case result, with the red lines marking the x-axis. The initial condition is shown in the left panel, with the color contour of the electric current density j_y component on the y=0, and z=0 planes. The current j_y =0 along the black lines, with kinks indicating changes in grid resolution. A gray plane is positioned at x= –320 Mm. The colored curves are current streamlines in 3-D: When the polarity of **j** is the same as the magnetic field (**j** ·**B** >0), it's colored in cyan, and white for opposite polarity (**j** ·**B** <0). The right panel

displays the same result at T=17h as shown in Figure 2b. However, electric current lines are plotted here instead of magnetic field lines.

In the middle of such a new CHFR, the magnetic field is predominantly poloidal, rendering the axial current negligible, and this region is no longer force-free. Thus, CHFRs are not stable and will dissipate. Starting from the center and propagating to both ends, the current system will rearrange. Correspondingly, the azimuthal magnetic field will gradually align towards the axial field. Ideally, the opposite helicity will annihilate, and a CHFR becomes a magnetic flux tube without any twist in its field. This annihilation will release all the energy of the azimuthal component of the magnetic field, which is about 1/6 of the total magnetic energy, as can be integrated from equation 1. Although this release occurs over an extended period, this amount of energy discharged from the entire MFR is orders of magnitude larger than that produced during the reconnection at the impact interface. This energy may contribute to particle acceleration or plasma heating and thus heats the solar wind. In the tranquil solar wind where plasma dynamics are minimal, the propagation speed of this alignment, estimated using the Alfvén speed, is typically below 0.1 times the solar wind speed. Consequently, a CHFR that passes through a detector within one hour, with its poloidal length scale exceeding its cross-section scale (large aspect ratio), could sustain for over 10 hours, offering sufficient opportunity for observation.

In our simulations of both the solar wind and magnetosheath environments, we assumed a 90° impact angle between the MFRs. This angle affects the relative field orientation across the interaction interface. Utilizing the same vector sketch approach as demonstrated in Figure 1, we find that both L-L and L-R configurations can lead to disentanglement across a range of impact angles, thereby supporting the production of CHFRs from IFRs.

Similarly, Linton et al. (2001) investigated MFR interactions in the low corona with a MHD code. They propelled uniformly twisted MFRs (Gold & Hoyle, 1960) in a solenoidal velocity field, achieving a disentanglement process that they call “slingshot”. We note that their product is an R-L CHFR (see their Figure 10). However, their parameters are normalized to magnetic field B_0 and MFR radius R_0, precluding a direct comparison with our Table 1. CHFRs can be found in their model results for impact angles between 90° and 270°. These results were later confirmed with a zero-β MHD simulation (Torok et al., 2011), to explain an indicated CHFR involved in an eruption on the solar surface (Chandra et al., 2010). On the other hand, most

studies on the interaction between MFRs focus on those whose axes are parallel to each other (e.g. Lau and Finn, 1996; Hansen et al., 2004, Zhao et al., 2015) to find multi-point interactions, where CHFRs are not evident.

MFRs with asymmetric helicity within their cross-sections have been suggested in the context of CMEs undergoing erosion via magnetic reconnection (Dasso et al., 2006; Pal et al., 2021). Additionally, MFRs with varying helicities along their axes, although unstable, have been proposed based on particle time-of-flight data in ICMEs (Cane et al., 1997; Owens et al., 2016). A recent multi-spacecraft observation, despite certain uncertainties, found opposite helicity from different parts of an ICME (Rodríguez-García et al., 2022). We recommend further examination of such cases because CHFR is a plausible, likely, and important phenomenon. Such investigations would expand our knowledge of MFRs in space plasmas.

The curvature and activities in the magnetosheath make MFRs complex and transient (e.g. Chen et al., 2017; Guo et al., 2021). Still, it's possible for one or a few spacecraft to cross the same curved MFR at different locations. When a spacecraft detects two shortly separated MFRs with identical plasma content but measures opposite chirality, it may be seeing a newly formed CHFR, providing another chance to observe CHFRs.

IFRs, a prerequisite condition for CHFRs generated in this study, are commonly observed in the inner heliosphere (Qi et al., 2020; Fargette et al., 2021). Additionally, the mixing of MFRs with opposite helicities, another condition for such CHFRs to form, is also available for small-scale MFRs in the solar wind (Zhao et al., 2021). However, identifying variable helicity along an MFR is challenging, given the determination of helicity from a single spacecraft measurement is notoriously challenging (Hu, 2017). Additionally, the concept of multiple MFRs winding around each other (Hu et al., 2004; Hwang et al., 2021, Figure 1e), MFRs with opposite helicity within their cross sections (Florido-Llinas et al., 2020), and MFR distortion (Nieves-Chinchilla et al, 2023) has been proposed, further acknowledging the complexity of MFRs in observation data. Nevertheless, with the increasing number of probes in the inner heliosphere, CHFRs may be observable through coherent observations from multiple spacecraft. Alternative methods of identification are also possible, like solar images (e.g. Zhang et al., 2012) and hints from in situ plasma data.

In addition to IFRs, direct emergence from the solar surface to generate CHFRs has been proposed when analyzing vector magnetograms (Vemareddy, 2021). Are there other processes to

form CHFRs in the solar wind? How often are they generated? More investigation is needed to answer such questions.

In summary, CHFRs have been identified in previous research, but their discussion has not been exhaustive. Focusing on a specific generation mechanism, we show the details of such structures to affirm their existence and highlight their significance. Additional theoretical and observational efforts are necessary across various regions of the inner heliosphere to comprehend the stability, evolution, and propagation of CHFRs. This study is significant for advancing our knowledge in solar wind heating and space weather, given the energy CHFRs release and the north-south magnetic flux they carry.

Acknowledgment

We acknowledge support from STEREO NASA award number 80NSSC21K1512, and MMS award number NNG04EB99C.

Data Availability Statement

The BARS-R-US code used in the study is available for download as a component of the Space Weather Modeling Framework at the University of Michigan (http://clasp.engin.umich.edu/swmf).

References

Belenkaya, E. S., Alexeev, I. I., Slavin, J. A., and Blokhina, M. S. (2013), Influence of the solar wind magnetic field on the Earth and Mercury magnetospheres in the paraboloidal model, Planet. Space Sci., 75, 46–55, DOI: 10.1016/j.pss.2012.10.013

Berger, M. A., Field, G. B. (1984), The topological properties of magnetic helicity, Journal of Fluid Mechanics, 147, DOI: https://doi.org/10.1017/S0022112084002019

Bothmer, V., Rust, D. M. (1997), The Field Configuration of Magnetic Clouds and the Solar Cycle, Geophysical Monograph Series 99, Coronal Mass Ejections, https://doi.org/10.1029/GM099p0139

Burlaga, L. ; Sittler, E. ; Mariani, F. ; Schwenn, R. (1981), Magnetic loop behind an interplanetary shock: Voyager, Helios, and IMP 8 observations, Journal of Geophysical Research, 86(A8), p. 6673-6684, DOI: 10.1029/JA086iA08p06673

Cane, H. V., Richardson, I. G., Wibberenz, G. (1997), Helios 1 and 2 observations of particle decreases, ejecta, and magnetic clouds, J. Geophys. Res., 102, A4, https://doi.org/10.1029/97JA00149

Chandra, R., Pariat, E., Schmeider, B., Mandrini, C. H., Uddin, W. (2010), How Can a Negative Magnetic Helicity Active Region Generate a Positive Helicity Magnetic Cloud? Solar Phys., 261, doi:10.1007/s11207-009-9470-2.

Chen, Y., Tóth, G., Cassak, P. et al. (2017), Global three-dimensional simulation of Earth's dayside reconnection using a two-way coupled magnetohydrodynamics with embedded particle-in-cell model: Initial results. Journal of Geophysical Research: Space Physics, 122, 10,318–10,335. https://doi.org/10.1002/2017JA024186

Dasso, S., Nakwacki, M. S., Démoulin, P. et al. (2006), A new model-independent method to compute magnetic helicity in magnetic clouds, Astronomy and Astrophysics, Volume 455, Issue 1, DOI: 10.1051/0004-6361:20064806

De Keyser, J., M. W. Dunlop, C. J. Owen, B. U. Ö. Sonnerup, S. E. Haaland, A. Vaivads, G. Paschmann, R. Lundin, and L. Rezeau (2005), Magnetopause and boundary layer, Space Sci. Rev., 118, 231–320, doi:10.1007/ s11214-005-3834-1

Fargette, N., Lavraud, B., Rouillard, A., et al. (2021). Magnetic increases with central current sheets: observations with Parker Solar Probe. Astronomy & Astrophysics, 650(A11). https://doi.org/10.1051/0004-6361/202039191

Florido-Llinas, M., Nieves-Chinchilla, T., Linton, M. G. (2020), Analysis of the Helical Kink Stability of Differently Twisted Magnetic Flux Ropes, Solar Phys., 295(9), DOI: 10.48550/arXiv.2007.06345

Forbes, T. G., Priest, E. R. (1995), Photospheric Magnetic Field Evolution and Eruptive Flares, Astrophys. J., 446, DOI: 10.1086/175797

Genestreti, K. J., Nakamura, T. K. M., Nakamura, R., E. R. et al. (2018), How Accurately Can We Measure the Reconnection Rate EM for the MMS Diffusion Region Event of 11 July 2017? J. Geophys. Res., 123, A11, DOI: 10.1029/2018JA025711

Gold T., F. Hoyle, On the Origin of Solar Flares, Monthly Notices of the Royal Astronomical Society, Volume 120, Issue 2, February 1960, Pages 89–105, https://doi.org/10.1093/mnras/120.2.89

Gopalswamy, N. (2004). A Global Picture of CMEs in the Inner Heliosphere. In: Poletto, G., Suess, S.T. (eds) The Sun and the Heliosphere as an Integrated System. Astrophysics and Space Science Library, vol 317. Springer, Dordrecht. https://doi.org/10.1007/978-1-4020-2831-1_8

Guo, Z., Lin, Y., & Wang, X. (2021). Global hybrid simulations of interaction between interplanetary rotational discontinuity and bow shock/magnetosphere: Can ion-scale magnetic reconnection be driven by rotational discontinuity downstream of quasi-parallel shock? Journal of Geophysical Research: Space Physics, 126, e2020JA028853. https://doi.Org/10.1029/2020JA028853

Hansen, J. F., Tripathi, S. K. P., Bellan, P. M. (2004), Co- and counter-helicity interaction between two adjacent laboratory prominences, Phys. Plasmas, 11. https://doi.org/10.1063/1.1724831

Hesse, M., Birn, J., & Schindler, K. (1990), On the topology of flux transfer events. Journal of Geophysical Research, 95(A5), 6549. https://doi.org/10.1029/ja095ia05p06549

Howard, T.A., Tappin, S.J. (2009), Interplanetary Coronal Mass Ejections Observed in the Heliosphere: 1. Review of Theory. Space Sci Rev 147, 31–54 https://doi.org/10.1007/s11214-009-9542-5

Hu, Q., C. W. Smith, N. F. Ness, and R. M. Skoug (2004), Multiple flux rope magnetic ejecta in the solar wind, J. Geophys. Res., 109, A03102, doi:10.1029/2003JA010101.

Hu, Q. The Grad–Shafranov Reconstruction of Toroidal Magnetic Flux Ropes: Method Development and Benchmark Studies. Sol Phys 292, 116 (2017). https://doi.org/10.1007/s11207-017-1134-z

Hu, Q., Zheng, J., Chen, Y., Roux, J., & Zhao, L. (2018). Automated Detection of Small-scale Magnetic Flux Ropes in the Solar Wind: First Results from the Wind Spacecraft Measurements. The Astrophysical Journal Supplement Series, 239(1). https://doi.org/10.3847/1538-4365/aae57d

Hwang, K.-J., Burch, J. L., Russell, C. T. et al. (2021), Microscale Processes Determining Macroscale Evolution of Magnetic Flux Tubes along Earth's Magnetopause, Astrophys. J., 914, 1, DOI 10.3847/1538-4357/abf8b1

Jia, X., Walker, R. J., Kivelson, M. G., et al. (2010), Dynamics of Ganymede's magnetopause: Intermittent reconnection under steady external conditions, J. Geophys. Res., 115, A12, https://doi.org/10.1029/2010JA015771

Jia, Y.-D., Qi, Y., Lu, S., & Russell, C. T. (2021). Temporal evolution of flux rope/tube entanglement in 3-D Hall MHD simulations. Journal of Geophysical Research: Space Physics, 126, e2020JA028698. https://doi.org/10.1029/2020JA028698

Jia, Y.-D., Hairong Lai, Nathan Miles, et al. (2023), Magnetic Field Enhancements in the Interplanetary Solar Wind: Diverse Processes Manifesting a Uniform Observation Type?. ESS Open Archive, DOI: 10.22541/essoar.170110674.49544737/v1

Lai, H. R., H. Y. Wei, C. T. Russell, C. S. Arridge, and M. K. Dougherty (2012), Reconnection at the magnetopause of Saturn: Perspective from FTE occurrence and magnetosphere size, J. Geophys. Res., 117, A05222, doi:10.1029/2011JA017263.

Lau, Y.-T., Finn, J. M. (1996), Magnetic reconnection and the topology of interacting twisted flux tubes, Physics of Plasmas, 3(11), DOI: 10.1063/1.871571

Linton, M. G., Dahlburg, R. B., & Antiochos, S. K. (2001). Reconnection of twisted flux tubes as a function of contact angle. The Astrophysical Journal, 553(2), 905–921. https://doi.org/10.1086/320974

Lundquist S (1950) Magneto-hydrodynamic fields. Ark Fys 2:361–365

Lu, S., Lu, Q. M., Cao, Y. et al. (2011), The effects of the guide field on the structures of electron density depletions in collisionless magnetic reconnection, Chinese Sci. Bull, 56, issue 1, DOI: 10.1007/s11434-010-4250-9

394 Manchester, W., Kilpua, E.K.J., Liu, Y.D. et al. The Physical Processes of CME/ICME
395 Evolution. Space Sci Rev 212, 1159–1219 (2017). https://doi.org/10.1007/s11214-017-
396 0394-0
397 McAllister, A. H., Martin, S. F., Crooker, N. U. et al. (2001), A test of real-time prediction of
398 magnetic cloud topology and geomagnetic storm occurrence from solar signatures, J.
399 Geophys. Res., 106, A12, https://doi.org/10.1029/2000JA000032
400 Moore, R. L., LaBonte, B. J. (1980), The filament eruption in the 3B flare of July 29, 1973 -
401 Onset and magnetic field configuration, in Solar and Interplanetary Dynamics; Proceedings
402 of the Symposium, Cambridge, Mass., (A81-27626 11-92) Dordrecht, D. Reidel Publishing
403 Co., 1980, p. 207-210; Discussion, p. 211.
404 Nieves-Chinchilla, T., M. A. Hidalgo, and H. Cremades (2023), Distorted-toroidal Flux Rope
405 Model, Astrophys. J., 947, 79, DOI 10.3847/1538-4357/acb3c1
406 Owens, M. J., Forsyth, R. J., Horbury, T. S., et al. (2016), DO THE LEGS OF MAGNETIC
407 CLOUDS CONTAIN TWISTED FLUX-ROPE MAGNETIC FIELDS? Astrophys. J., 818,
408 50, DOI: 10.3847/0004-637X/818/2/197
409 Pal, S., Kilpua, R., Good, S. (2021), Uncovering erosion effects on magnetic flux rope twist,
410 Astron. Astrophys., 650, A176, https://doi.org/10.1051/0004-6361/202040070
411 Pal, S. (2022), Uncovering the process that transports magnetic helicity to coronal mass ejection
412 flux ropes, Adv. Space Res., 70, 6, https://doi.org/10.1016/j.asr.2021.11.013
413 Pritchett, P. L., and F. V. Coroniti (2004), Three-dimensional collisionless magnetic
414 reconnection in the presence of a guide field, J. Geophys. Res., 109, A01220,
415 doi:10.1029/2003JA009999.
416 Qi, Y., Russell, C. T., Jia, Y.-D., & Hubbert, M. (2020). Temporal evolution of flux tube
417 entanglement at the magnetopause as observed by the MMS satellites. Geophysical
418 Research Letters, 47, e2020GL090314. https://doi.org/10.1029/2020GL090314
419 Qiu, J., Hu, Q., Howard, T. A., Yurchyshyn, V. B. (2007), On the Magnetic Flux Budget in Low-
420 Corona Magnetic Reconnection and Interplanetary Coronal Mass Ejections, Astrophys. J.,
421 659(1), DOI: 10.1086/512060
422 L. Rodríguez-García, T. Nieves-Chinchilla, R. Gómez-Herrero et al., (2022), Evidence of a
423 complex structure within the 2013 August 19 coronal mass ejection, A&A 662(A45), DOI:
424 https://doi.org/10.1051/0004-6361/202142966

425 Russell, C. T., Elphic, R. (1979a), ISEE observations of flux transfer events at the dayside
426 magnetopause, Geophys. Res. Lett., 6, 1, DOI: 10.1029/GL006i001p00033
427 Russell, C. T., Elphic, R. (1979b), Observation of magnetic flux ropes in the Venus ionosphere,
428 Nature, 279, DOI: 10.1038/279616a0
429 Solov'ev, A. A., Kirichek, E. A. (2021), Properties of the Flare Energy Release in Force-Free
430 Magnetic Flux Ropes, Mon. Not. R. Astron. Soc., 505,
431 https://doi.org/10.1134/s1063773723050055
432 Tharp T, Yamada M, Ji H et al. (2012) Quantitative study of guide-field effects on Hall
433 reconnection in a laboratory plasma. Phys Rev Lett 109:169002,
434 https://doi.org/10.1103/PhysRevLett.109.165002
435 Thompson W.T. (2013), Alternating Twist Along an Erupting Prominence, Solar Phys, 283:489–
436 504, DOI 10.1007/s11207-013-0228-5
437 Torok, T., Chandra, R., Pariat, E. et al. (2011), FILAMENT INTERACTION MODELED BY
438 FLUX ROPE RECONNECTION, Astrophys. J., 728, 65, DOI 10.1088/0004-
439 637X/728/1/65
440 Tóth, G., Ma, Y. J., & Gombosi, T. I. (2008). Hall magnetohydrodynamics on block-adaptive
441 grids. Journal of Computational Physics, 227(14), 6967–6984.
442 https://doi.org/10.1016/j.jcp.2008.04.010
443 Tóth, G., van der Holst, B., Sokolov, I. V., De Zeeuw, D. L., Gombosi, T. I., Fang, F., et al.
444 (2012). Adaptive numerical algorithms in space weather modeling. Journal of
445 Computational Physics, 231(3), 870–903. https://doi.org/10.1016/j.jcp.2011.02.006
446 Ulrich, R. K., Riley, P., Tran, T. (2018), Solar Sources of Interplanetary Magnetic Clouds
447 Leading to Helicity Prediction, Space Weather, 16, 11,
448 https://doi.org/10.1029/2018SW001912
449 Vemareddy, P. (2021), Successive injection of opposite magnetic helicity: evidence for active
450 regions without coronal mass ejections, Mon. Not. R. Astron. Soc., 507.
451 https://doi.org/10.1093/mnras/stab2401
452 Wang, X. Y., Lin, Y., & Chang, S.-W. (2009). Hybrid simulation of foreshock waves and ion
453 spectra and their linkage to cusp energetic ions. Journal of Geophysical Research, 114(A6),
454 A06203. https://doi.org/10.1029/2008JA013745

Zhang, J., Cheng, X. & Ding, Md. Observation of an evolving magnetic flux rope before and during a solar eruption. Nat Commun 3, 747 (2012). https://doi.org/10.1038/ncomms1753

Zhao, L., DeVore, C. R., Antiochos, S. K. (2015), NUMERICAL SIMULATIONS OF HELICITY CONDENSATION IN THE SOLAR CORONA, Astrophys. J., 805:61, DOI 10.1088/0004-637X/805/1/61

Zhao, L.-L., G. P. Zank, Q. Hu, et al. (2021). Detection of small magnetic flux ropes from the third and fourth Parker Solar Probe encounters. Astronomy & Astrophysics, 650(A12). https://doi.org/10.1051/0004-6361/202039298